LETTER TO THE EDITOR

Mapping the hot gas temperature in galaxy clusters using X-ray and Sunyaev-Zel'dovich imaging

R. Adam[1,2]*, M. Arnaud[3], I. Bartalucci[3], P. Ade[4], P. André[3], A. Beelen[5], A. Benoît[6], A. Bideaud[4], N. Billot[7], H. Bourdin[8], O. Bourrion[2], M. Calvo[6], A. Catalano[2], G. Coiffard[9], B. Comis[2], A. D'Addabbo[6,10], F.-X. Désert[11], S. Doyle[4], C. Ferrari[1], J. Goupy[6], C. Kramer[7], G. Lagache[12], S. Leclercq[9], J.-F. Macías-Pérez[2], S. Maurogordato[1], P. Mauskopf[4,13], F. Mayet[2], A. Monfardini[6], F. Pajot[5], E. Pascale[4], L. Perotto[2], G. Pisano[4], E. Pointecouteau[14,15], N. Ponthieu[11], G.W. Pratt[3], V. Revéret[3], A. Ritacco[2], L. Rodriguez[3], C. Romero[9], F. Ruppin[2], K. Schuster[9], A. Sievers[7], S. Triqueneaux[6], C. Tucker[4], and R. Zylka[9]

[1] Laboratoire Lagrange, Université Côte d'Azur, Observatoire de la Côte d'Azur, CNRS, Blvd de l'Observatoire, CS 34229, 06304 Nice cedex 4, France
[2] Laboratoire de Physique Subatomique et de Cosmologie, Université Grenoble Alpes, CNRS/IN2P3, 53, avenue des Martyrs, Grenoble, France
[3] Laboratoire AIM, CEA/IRFU, CNRS/INSU, Université Paris Diderot, CEA-Saclay, 91191 Gif-Sur-Yvette, France
[4] Astronomy Instrumentation Group, University of Cardiff, UK
[5] Institut d'Astrophysique Spatiale (IAS), CNRS and Université Paris Sud, Orsay, France
[6] Institut Néel, CNRS and Université Grenoble Alpes, France
[7] Institut de RadioAstronomie Millimétrique (IRAM), Granada, Spain
[8] Dipartimento di Fisica, Università degli Studi di Roma 'Tor Vergata', via della Ricerca Scientifica, 1, I-00133 Roma, Italy
[9] Institut de RadioAstronomie Millimétrique (IRAM), Grenoble, France
[10] Dipartimento di Fisica, Sapienza Università di Roma, Piazzale Aldo Moro 5, I-00185 Roma, Italy
[11] Institut de Planétologie et d'Astrophysique de Grenoble (IPAG), CNRS and Université Grenoble Alpes, France
[12] Aix Marseille Université, CNRS, LAM (Laboratoire d'Astrophysique de Marseille) UMR 7326, 13388, Marseille, France
[13] School of Earth and Space Exploration and Department of Physics, Arizona State University, Tempe, AZ 85287
[14] Université de Toulouse, UPS-OMP, Institut de Recherche en Astrophysique et Planétologie (IRAP), Toulouse, France
[15] CNRS, IRAP, 9 Av. colonel Roche, BP 44346, F-31028 Toulouse cedex 4, France

ABSTRACT

We propose an alternative method to map the temperature distribution of the hot gas in galaxy clusters that uses resolved images of the thermal Sunyaev-Zel'dovich (tSZ) effect in combination with X-ray data. Application of the method to images from the New IRAM KIDs Array (NIKA) and XMM-*Newton* allows us to measure the gas temperature and determine its spatial distribution in the merging cluster MACS J0717.5+3745, at $z = 0.55$. Despite the complexity of the target cluster, we find a good morphological agreement between the temperature maps derived from X-ray spectroscopy only – using XMM-*Newton* (T_{XMM}) and *Chandra* (T_{CXO}) – and the new gas-mass-weighted tSZ+X-ray imaging method (T_{gmw}). We correlate the temperatures from tSZ+X-ray imaging and those from X-ray spectroscopy alone, providing an independent temperature cross calibration. We find a good agreement between T_{gmw} and T_{XMM}, while T_{CXO} is higher by $\sim 15\%$. Our results are limited by uncertainties in the geometry of the cluster gas and kinetic SZ contamination ($\sim 10\%$), and the absolute calibration of the tSZ map (7%). Investigation using a larger sample of clusters would minimize these effects.

Key words. Techniques: high angular resolution – Galaxies: clusters: individual: MACS J0717.5+3745; intracluster medium – X-rays: galaxies: clusters

1. Introduction

The temperature and density are the key observable characteristics of the hot ionized gas in the intracluster medium (ICM) of galaxy clusters. X-ray observations have historically played a fundamental role in their measurement: the density is trivial to obtain from X-ray imaging, while the temperature can be derived from an isothermal model fit to the spectrum. Accurate gas temperatures are needed for a number of reasons. They are essential to infer cluster masses under the assumption of hydrostatic equilibrium (Sarazin 1988); in turn, these masses can be used to infer con-

straints on cosmological parameters (e.g., Allen et al. 2011). The temperature structure yields information on the detailed physics of shock-heated gas in merging events, the nature of cold fronts, and the role of turbulence and gas sloshing (see e.g. Markevitch & Vikhlinin 2007, for a review). In turn, such analyses provide insights into the physics of galaxy clusters, which is necessary to interpret the scaling relations between clusters masses and their primary observables (Khedekar et al. 2013).

However, the X-ray gas temperature measurement is potentially affected by two systematic effects. First, the X-ray emission is proportional to the square of the ICM electron density, such that spectroscopic temperatures are driven by the colder, denser,

regions along the line-of-sight, and are thus sensitive to gas clumping. What is measured is in fact a weighted mean temperature, where the weight is a non-linear combination of the temperature and density structure (see e.g. Mazzotta et al. 2004; Vikhlinin 2006). Numerical simulations support this view (e.g. Nagai et al. 2007; Rasia et al. 2014), but estimates of the magnitude of any bias due to this effect vary widely depending on the numerical scheme (e.g. smoothed particle hydrodynamics, adaptive mesh refinement) and the details of the 'sub-grid' physics (cooling, feedback, etc). Secondly, the spectroscopic temperatures depend directly on the energy calibration of X-ray observatories. For instance, X-ray temperatures obtained with *Chandra* are generally higher than those measured by XMM-*Newton*, by up to a factor of 15% at 10 keV (e.g., Mahdavi et al. 2013).

The thermal Sunyaev-Zel'dovich (tSZ, Sunyaev & Zeldovich 1972) effect is related to the mean gas-mass-weighted temperature along the line-of-sight and the electron density, via the ideal gas law. The tSZ effect can thus be used to obtain an alternative estimate of the gas temperature, provided a measure of the density is available. Combination of the tSZ and X-ray observations can then in principle be used to decouple temperature and density in each individual measurement. Here we use deep, resolved (< 20″) tSZ observations, combined with X-ray imaging, to measure the spatial distribution of the gas temperature toward the merging cluster MACS J0717.5+3745 at $z = 0.55$. We have chosen MACS J0717.5+3745 because it is one of the very few objects for which sufficiently deep and resolved tSZ data are currently available (Adam et al. 2016a). The complex morphology of the cluster is the primary limiting factor to our analysis; however it allows us to explore a wide range of gas temperatures, which will not necessarily be accessible with more simple objects.

We assume a flat ΛCDM cosmology according to the latest *Planck* results (Planck Collaboration et al. 2015) with $H_0 = 67.8$ km s^{-1} Mpc^{-1}, $\Omega_M = 0.308$, and $\Omega_\Lambda = 0.692$. At the cluster's redshift, 1 arcsec corresponds to 6.6 kpc.

2. Data

The New IRAM KIDs Array (NIKA, see Monfardini et al. 2011; Calvo et al. 2013; Adam et al. 2014; Catalano et al. 2014) has observed MACS J0717.5+3745 at 150 and 260 GHz for a total of 47.2 ks. The main steps of the data reduction are described in Adam et al. (2015, 2016b,a); Ruppin et al. (2016). In this paper, we use the NIKA 150 GHz tSZ map at 22 arcsec effective angular resolution FWHM, deconvolved from the transfer function except for the beam smoothing. The overall calibration uncertainty is estimated to be 7%, including the brightness temperature model of our primary calibrator, the NIKA bandpass uncertainties, the opacity correction, and the stability of the instrument (Catalano et al. 2014). The absolute zero level for the brightness on the map remains unconstrained by NIKA. MACS J0717.5+3745 is contaminated by a significant amount of kinetic SZ (kSZ, Sunyaev & Zeldovich 1980) signal and we used the best-fit model F2 from Adam et al. (2016a) to remove its contribution. This model has large uncertainties but it still allows us to test the impact of the kSZ effect on our results.

MACS J0717.5+3745 was observed several times by the XMM-*Newton* and *Chandra* X-ray observatories (obs-IDs 0672420101, 0672420201, 067242030, and 800123, 800356, 801417, 801432, respectively). The data processing follows the description given in Adam et al. (2016a). The clean exposure time is 153 ks for *Chandra* and 160 and 116 ks for XMM-*Newton* MOS1,2 and PN cameras, respectively.

3. Temperature reconstruction

The X-ray spectroscopic temperature maps from *Chandra* ($\bar{T}_{\rm CXO}$) and XMM-*Newton* ($\bar{T}_{\rm XMM}$) were produced using the wavelet filtering algorithm described in Bourdin & Mazzotta (2008), as detailed in Adam et al. (2016a). As the significance of wavelet coefficients partly depends on the photon count statistics, the effective resolution varies across the map, XMM-*Newton* allowing a finer sampling than *Chandra* due to the higher effective area. Note that the nature of the algorithm does not allow a direct calculation of the temperature map uncertainties. From jackknife resampling of the individual observations (each spanning $\sim 1/3$ of the total exposure time), we conservatively estimate statistical uncertainties of $\sim 14\%$ for XMM-*Newton* and $\sim 29\%$ for *Chandra*. The method employed to recover the temperature of the gas from NIKA tSZ and XMM-*Newton* X-ray imaging, $\bar{T}_{\rm gmw}$ is described below.

3.1. Primary observables

The tSZ signal, measured at frequency ν, can be expressed as

$$\frac{\Delta I_\nu}{I_0} = f(\nu, T_e)\frac{\sigma_{\rm T}}{m_e c^2}\int P_e dl \equiv k_{\rm B}\bar{T}_{\rm gmw} f(\nu, T_e)\frac{\sigma_{\rm T}}{m_e c^2}\int n_e dl,$$
(1)

where $f(\nu, T_e)$ is the tSZ spectrum, which depends slightly on temperature T_e in the case of very hot gas. The signal is proportional to the line-of-sight integrated electron pressure, P_e. It is related to the mean gas-mass-weighted temperature along the line-of-sight, $\bar{T}_{\rm gmw} \equiv \frac{\int T_e n_e dl}{\int n_e dl}$, and the electron density, n_e, via the ideal gas law. The X-ray surface brightness is driven by the electron density:

$$S_{\rm X} = \frac{1}{4\pi(1+z)^4}\int n_e^2 \Lambda(T_e, Z)\, dl.$$
(2)

where z is the cluster redshift, and $\Lambda(T_e, Z)$ is the emissivity in the relevant energy band, taking into account the interstellar absorption and the instrument spectral response. $\Lambda(T_e, Z)$ depends only weakly on the temperature and metallicity of the gas Z, so that instrumental systematics have a negligible impact on the results presented in this paper.

3.2. X-ray electron density mapping

We use the XMM-*Newton* X-ray surface brightness (equation 2) to produce a map of the square of the electron density integrated along the line-of-sight. To combine it with tSZ observations, we have to convert $\int n_e^2 dl$ to $\int n_e dl$ via an effective electron depth, expressed as

$$\ell_{\rm eff} = \frac{\left(\int n_e dl\right)^2}{\int n_e^2 dl}.$$
(3)

From Eq. 2, the effective electron density along the line-of-sight is then given by

$$\bar{n}_e = \frac{1}{\ell_{\rm eff}}\int n_e dl = \frac{1}{\ell_{\rm eff}}\sqrt{\ell_{\rm eff}\frac{4\pi(1+z)^4 S_{\rm X}}{\Lambda(T_e, Z)}}.$$
(4)

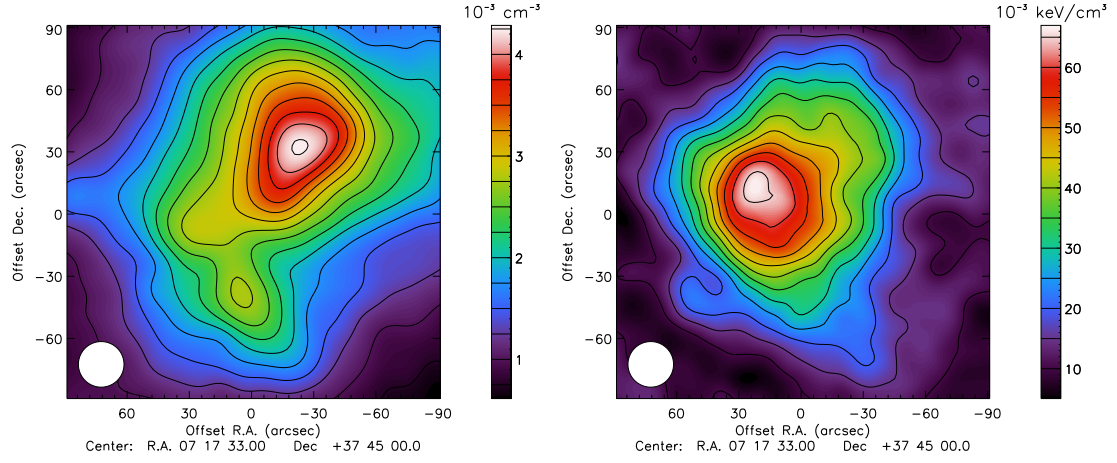We use several approaches to estimate $\ell_{\rm eff}$ and its uncertainty:

Fig. 1. Left: effective line-of-sight integrated electron density, $\bar{n}_e$, derived from XMM-*Newton*. **Right**: effective line-of-sight integrated pressure, $\bar{P}_e$, derived from NIKA. These maps correspond to model M1, and were smoothed with a Gaussian kernel to an effective resolution of 22 arcsec FWHM. The pressure map is cleaned from our best-fit kSZ model and corrected for the zero level.
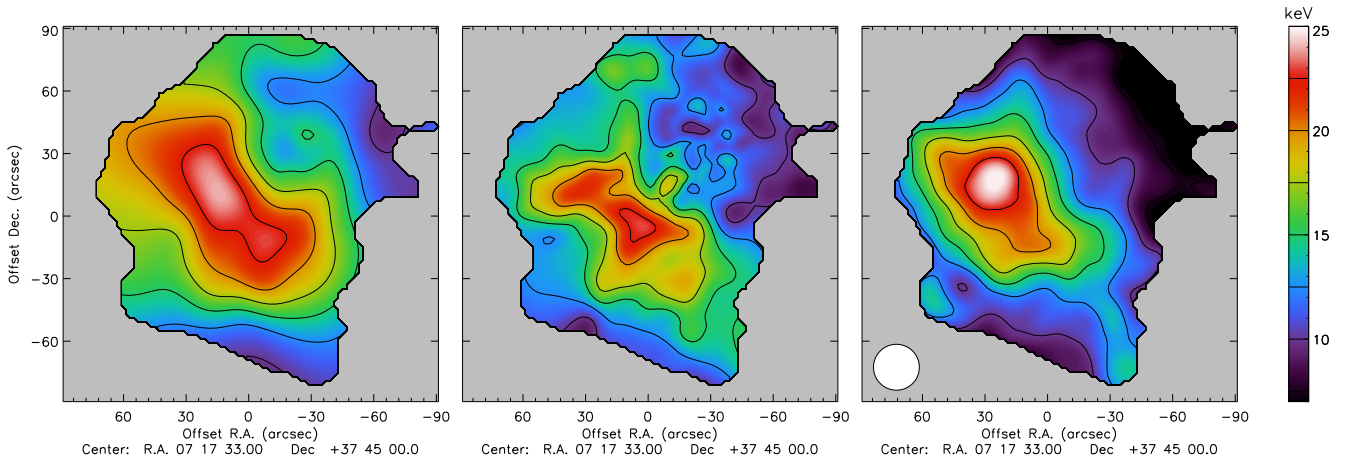

Fig. 2. Left: *Chandra* derived spectroscopic temperature map, $\bar{T}_{CXO}$. **Middle**: XMM-*Newton* derived spectroscopic temperature map, $\bar{T}_{XMM}$. **Right**: NIKA+XMM-*Newton* imaging derived temperature map for model M1, $\bar{T}_{gmw}$. This map is corrected for the zero level.

1. **Model M1** Following Sayers et al. (2013), we assume that ℓ_{eff} is constant at $\ell_{eff} = 1400$ kpc, as estimated by Mroczkowski et al. (2012), across the cluster extension.

2. **Model M2** We derive an electron density profile from deconvolution and deprojection of the XMM-*Newton* radial S_X profile centered on the X–ray peak (Croston et al. 2006), thus obtaining an azimuthally symmetric ℓ_{eff} map.

3. **Model M3** We use the best fitting NIKA tSZ+XMM-*Newton* density model of Adam et al. (2016a), which accounts for the four main subclusters in MACS J0717.5+3745, to compute a map of ℓ_{eff}. The model does not constrain the line-of-sight distance between the subclusters because the tSZ signal depends linearly on the density. Therefore, we consider two extreme cases: **M3a)** where the subclusters are sufficiently far away from each other such that $\int n_e^2 dl \simeq \sum_j \int n_{e,j}^2 dl$, where j refers to each subcluster; **M3b)** where all the subclusters are located at the same line-of-sight coordinate, i.e. the same redshift, such that the physical distance between the subclusters are minimal.

The internal structure of MACS J0717.5+3745 is increasingly refined from model M1 to M3, but we find good consistency between all three models. Model M2 presents a minimum of 1200 kpc toward the X-ray center and increases quasi-linearly

toward higher radii, reaching about 2000 kpc at 1 arcmin, in line with expectations from model M1. Model M3a is minimal in the central region, in the direction of the subclusters (~ 1200 kpc), and also increases with radius. Model M3b provides a lower limit for ℓ_{eff}, increasing from ~ 800 kpc near the center to ~ 1200 kpc at 1 arcmin. The left panel of Figure 1 represents the $\bar{n}_e$ map in the case of model M1.

3.3. Thermal Sunyaev-Zel'dovich pressure mapping

We can express the effective pressure along the line-of-sight directly from equation 1, as

$$\bar{P}_e = \frac{1}{\ell_{eff}} \int P_e dl = \frac{m_e c^2}{\sigma_T} \frac{y_{tSZ}}{\ell_{eff}}. \qquad (5)$$

This quantity is straightforwardly obtained from the NIKA map accounting for relativistic corrections as detailed in Adam et al. (2016a). As the temperature can be very high, the relativistic corrections are non negligible (Pointecouteau et al. 1998; Itoh & Nozawa 2003), but the exact choice of the temperature map used to apply relativistic corrections has a negligible impact on our results (i.e., $\bar{T}_{XMM}$, $\bar{T}_{CXO}$ or $\bar{T}_{gmw}$). The right panel of Figure 1 presents the $\bar{P}_e$ map in the case of model M1 corrected for kSZ and zero level. (see Section 4.2).

3.4. Gas-mass-weighted temperature mapping

The tSZ+X-ray imaging temperature map, referred to as gas-mass-weighted, is obtained by combining the effective density and the effective pressure:

$$k_B \bar{T}_{gmw} \equiv \frac{\int k_B T_e n_e dl}{\int n_e dl} = \frac{\bar{P}_e}{\bar{n}_e} = \frac{m_e c^2}{\sigma_T} \sqrt{\frac{\Lambda(T_e, Z)}{4\pi (1+z)^4 \ell_{eff} S_X}} y_{tSZ}.$$

(6)

We propagate the noise arising from the tSZ map and the X-ray surface brightness using Monte Carlo realizations; the overall noise on $\bar{T}_{gmw}$ is dominated by that of the tSZ map.

4. Results

4.1. Morphology

Figure 2 shows the three temperature maps $\bar{T}_{CXO}$, $\bar{T}_{XMM}$, and $\bar{T}_{gmw}$ for model M1. $\bar{T}_{gmw}$ is kSZ-corrected, and corrected for the zero level. They all identify a hot gas 'bar' to the southeast. The position of the temperature peak is the same for $\bar{T}_{CXO}$ and $\bar{T}_{gmw}$, while it is slightly shifted southwest for $\bar{T}_{XMM}$; however it also coincides with a region where kSZ contamination is large, leading to possible overestimation in $\bar{T}_{gmw}$. All three maps indicate cooler temperatures in the the northwest sector. Varying the kSZ correction and the ℓ_{eff} models slightly changes the morphology of $\bar{T}_{gmw}$ locally, but the agreement with X-ray spectroscopy is good in all cases.

4.2. Temperature comparison

Figure 3 shows the correlation between the maps shown in Figure 2. The temperature values are extracted in each 10 arcsec pixel, where the resolution of the $\bar{T}_{gmw}$ map is 22 arcsec. We mask pixels where the tSZ signal-to-noise ratio is lower than 2 to avoid possible bouncing effects on the edge of the map due to the NIKA data processing.

Since the zero level of the tSZ map is unconstrained, we express the effective pressure map as $\bar{P}_e = \bar{P}_{true} + \bar{P}_0$, where $\bar{P}_0$ is an unknown offset. Following equation 6, the gas-mass-weighted temperature can then be expressed with respect to the spectroscopic temperature, as

$$k_B \bar{T}_{gmw} = \alpha_{gmw-X} \times k_B \bar{T}_{XMM/CXO} + \beta/\bar{n}_e,$$

(7)

where α_{gmw-X} is a cross-calibration term and β gives a measurement of $\bar{P}_0$. For X-ray spectroscopic temperatures, we simply write $T_{XMM} = \alpha_{XMM-CXO} \times T_{CXO}$. Table 1 gives the α coefficients obtained using a χ^2 fit for the different ℓ_{eff} models tested, and their dependence on the kSZ correction. The scatter, σ, is the standard deviation of the residual between the values and the best-fit relation.

The scatter of about 2 keV between $\bar{T}_{CXO}$ and $\bar{T}_{XMM}$ is dominated by statistical error, and also by the differences in the scales probed by the two maps. The scatters between $\bar{T}_{gmw}$ and both X-ray temperatures are comparable. This is not compatible with the noise as propagated into the T_{gmw} map, and may be due to a number of factors, including spectroscopic temperature noise, the difference in angular resolution of the maps, or an intrinsic scatter between gas-mass-weighted and spectroscopic temperatures.

The tSZ+X-ray imaging versus X-ray only cross-calibration is stable to within less than 10%, depending on the choice of the ℓ_{eff} model and the kSZ correction used, while the statistical

Table 1. Regression and scatter coefficients between the temperature maps. The statistical uncertainties on α coefficients are 2%. *Model M3b gives a lower limit for ℓ_{eff}, and thus should be taken only as an upper limit for α.

Slope / scatter (keV)	M1	M2	M3a	M3b*
	ℓ_{eff} model			
	kSZ-uncorrected			
$(\alpha, \sigma)_{gmw-XMM}$	(1.07, 1.9)	(1.00, 2.0)	(0.96, 2.2)	(1.56, 2.8)
$(\alpha, \sigma)_{gmw-CXO}$	(0.93, 1.9)	(0.90, 1.9)	(0.76, 2.6)	(1.34, 2.6)
	kSZ-corrected			
$(\alpha, \sigma)_{gmw-XMM}$	(1.03, 2.7)	(1.00, 2.3)	(0.97, 2.4)	(1.43, 4.4)
$(\alpha, \sigma)_{gmw-CXO}$	(0.89, 2.6)	(0.89, 2.1)	(0.77, 2.8)	(1.23, 4.2)
$(\alpha, \sigma)_{XMM-CXO}$	(0.85, 2.0)			

uncertainties are 2%. The cross-calibration coefficients also directly depend on the absolute calibration of the tSZ map, which is expected to be accurate within 7%. Model M3b provides a lower limit on ℓ_{eff}, and therefore an upper limit on α_{gmw-X}.

5. Discussion and conclusions

Using deep tSZ observations together with X-ray imaging, we have extracted an ICM temperature map of the galaxy cluster MACS J0717.5+3745. This map is gas-mass-weighted and provides an alternative to X-ray spectroscopic based methods. The test cluster being extremely hot, with the peak temperature reaching up to ~ 25 keV, it allows us to sample a large range of temperature, which would not be accessible with the large majority of clusters.

The morphological comparison of the gas-mass-weighted temperature map to XMM-*Newton* and *Chandra* X-ray spectroscopic maps indicates good agreement between the different methods. All three maps are consistent with MACS J0717.5+3745 being cold on the northwest region and presenting a bar-like temperature structure to the southeast, indicative of heating from adiabatic compression owing to the merger between two main subclusters (see, e.g., Ma et al. 2009).

Figure 3 and Table 1 indicate that *Chandra* temperatures are about 15% higher than those of XMM-*Newton*, as found by previous work (Mahdavi et al. 2013; Schellenberger et al. 2015), while $\bar{T}_{gmw}$ and $\bar{T}_{XMM}$ are in good agreement. We should avoid over-interpretation of this result in terms of absolute calibration. The gas-mass-weighted temperature map we have derived is limited by the complexity of the test cluster and assumptions on the effective electron depth of the ICM, kSZ contamination, and the calibration of the NIKA instrument. For a perfectly spherical cluster, the ratio T_X/T_{gmw} would give access to absolute calibration of the X-ray temperature. Clusters being complex objects, the ratio we really measure is a complicated combination of the 3D temperature structure and intrinsic properties affecting the density such as amount of substructure, gas clumpiness and triaxiality. A larger sample would allow us to disentangle instrumental calibration from effects linked to intrinsic cluster properties.

We note that the noise in our T_{gmw} map is comparable to that obtained from XMM-*Newton* and *Chandra*, but obtained with a factor of three smaller observing time. This illustrates the potential of resolved tSZ observations at intermediate to high redshifts, where X-ray spectroscopy becomes challenging, and which should be routinely provided by the up-coming generation of SZ instruments, MUSTANG2 (Dicker et al. 2014) and NIKA2 (Calvo et al. 2016; Comis et al. 2016).
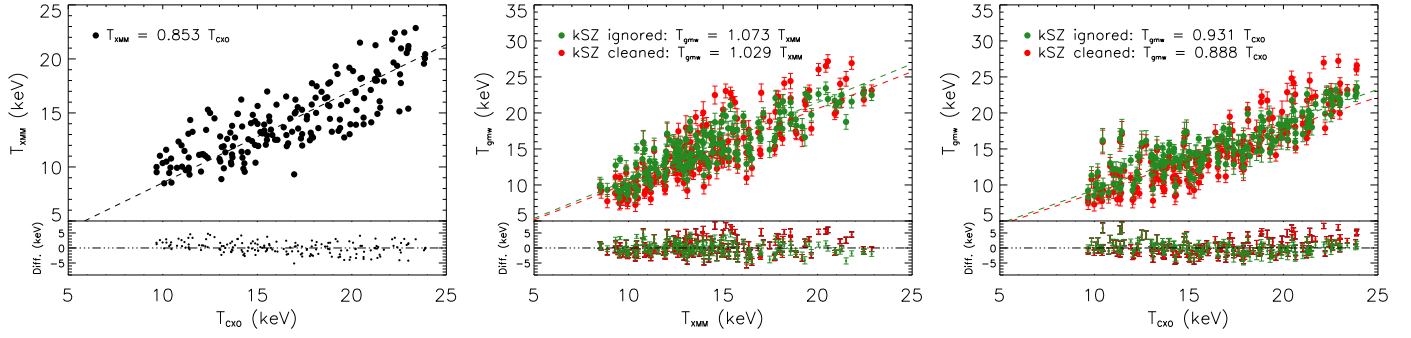
Fig. 3. Correlation between the temperature maps of Figure 2 and residual. **Left:** XMM-*Newton* versus *Chandra* spectroscopic temperatures. **Middle:** tSZ+X-ray imaging (model M1) versus XMM-*Newton* spectroscopy. **Right:** tSZ+X-ray imaging (model M1) versus *Chandra* spectroscopy. The red and green dots correspond to the case with and without the kSZ correction, respectively.

References

Adam, R. et al. 2016a, ArXiv e-prints, 1606.07721
——. 2016b, A&A, 586, A122, 1510.06674
——. 2015, A&A, 576, A12, 1410.2808
——. 2014, A&A, 569, A66, 1310.6237
Allen, S. W., Evrard, A. E., & Mantz, A. B. 2011, ARA&A, 49, 409, 1103.4829
Bourdin, H., & Mazzotta, P. 2008, A&A, 479, 307, 0802.1866
Calvo, M. et al. 2016, Journal of Low Temperature Physics, 1601.02774
——. 2013, A&A, 551, L12
Catalano, A. et al. 2014, A&A, 569, A9, 1402.0260
Comis, B. et al. 2016, ArXiv e-prints, 1605.09549
Croston, J. H., Arnaud, M., Pointecouteau, E., & Pratt, G. W. 2006, A&A, 459, 1007, astro-ph/0608700
Dicker, S. R. et al. 2014, in Proc. SPIE, Vol. 9153, Millimeter, Submillimeter, and Far-Infrared Detectors and Instrumentation for Astronomy VII, 91530J
Itoh, N., & Nozawa, S. 2003, ArXiv Astrophysics e-prints, astro-ph/0307519
Khedekar, S., Churazov, E., Kravtsov, A., Zhuravleva, I., Lau, E. T., Nagai, D., & Sunyaev, R. 2013, MNRAS, 431, 954, 1211.3358
Ma, C.-J., Ebeling, H., & Barrett, E. 2009, ApJ, 693, L56, 0901.4783
Mahdavi, A., Hoekstra, H., Babul, A., Bildfell, C., Jeltema, T., & Henry, J. P. 2013, ApJ, 767, 116, 1210.3689
Markevitch, M., & Vikhlinin, A. 2007, Phys. Rep., 443, 1, astro-ph/0701821
Mazzotta, P., Rasia, E., Moscardini, L., & Tormen, G. 2004, MNRAS, 354, 10, astro-ph/0404425
Monfardini, A. et al. 2011, ApJS, 194, 24, 1102.0870
Mroczkowski, T. et al. 2012, ApJ, 761, 47, 1205.0052
Nagai, D., Vikhlinin, A., & Kravtsov, A. V. 2007, ApJ, 655, 98, astro-ph/0609247
Planck Collaboration et al. 2015, ArXiv e-prints, 1502.01589
Pointecouteau, E., Giard, M., & Barret, D. 1998, A&A, 336, 44, astro-ph/9712271
Rasia, E. et al. 2014, ApJ, 791, 96
Ruppin, F. et al. 2016, ArXiv e-prints, 1607.07679
Sarazin, C. L. 1988, X-ray emission from clusters of galaxies
Sayers, J. et al. 2013, ApJ, 778, 52, 1312.3680
Schellenberger, G., Reiprich, T. H., Lovisari, L., Nevalainen, J., & David, L. 2015, A&A, 575, A30, 1404.7130
Sunyaev, R. A., & Zeldovich, I. B. 1980, MNRAS, 190, 413
Sunyaev, R. A., & Zeldovich, Y. B. 1972, Comments on Astrophysics and Space Physics, 4, 173
Vikhlinin, A. 2006, ApJ, 640, 710, astro-ph/0504098